The axial ratio of hcp Fe and Fe–Ni–Si alloys to the conditions of Earth's inner core

Rebecca A. Fischer* and Andrew J. Campbell

Department of the Geophysical Sciences, University of Chicago, 5734 S Ellis Ave, Chicago, IL 60637, USA

*Corresponding author. Email: rfischer@uchicago.edu

Accepted for publication in *American Mineralogist* (Building Planets), 27 May 2015

Abstract

The Earth's iron-rich inner core is seismically anisotropic, which may be due to the preferred orientation of Fe-rich hexagonal close packed (hcp) alloy crystals. Elastic anisotropy in a hexagonal crystal is related to its *c*/*a* axial ratio; therefore, it is important to know how this ratio depends on volume (or pressure), temperature, and composition. Experimental data on the axial ratio of iron and alloys in the Fe–Ni–Si system from 15 previous studies are combined here to parameterize the effects of these variables. The axial ratio increases with increasing volume, temperature, silicon content, and nickel content. When an hcp phase coexists with another structure, sample recovery and chemical analysis from each pressure-temperature point is one method for determining the phase's composition and thus the position of the phase boundary. An alternate method is demonstrated here, using this parameterization to calculate the composition of an hcp phase whose volume, temperature, and axial ratio are measured. The hcp to hcp+B2 phase boundary in the Fe–FeSi system is parameterized as a function of pressure, temperature, and composition, showing that a silicon-rich inner core may be an hcp+B2 mixture. These

findings could help explain observations of a layered seismic anisotropy structure in the Earth's inner core.

Introduction

In the upper part of the Earth's iron-rich inner core, seismic waves traveling parallel to the planet's rotational axis propagate ~3% faster than waves traveling in the equatorial plane (Morelli et al. 1986; Poupinet et al. 1983). Seismic data suggest the existence of layered structures and hemispherical variations of this anisotropy (e.g., Irving and Deuss 2011a, 2011b; Ishii and Dziewonski 2002, 2003; Lythgoe et al. 2014; Tanaka and Hamaguchi 1997). Numerous mechanisms for explaining these properties have been considered (e.g., Alboussière et al. 2010; Bergman 1997; Buffett and Wenk 2001; Jeanloz and Wenk 1988; Karato 1999; Reaman et al. 2011; Yoshida et al. 1996). This anisotropy is frequently attributed to preferred orientation of Fe-rich alloy crystals in the inner core, due to iron's strong single-crystal elastic anisotropy (Jeanloz and Wenk 1988; Morelli et al. 1986; Stixrude and Cohen 1995). The c/a axial ratio of a hexagonal crystal directly influences its elastic anisotropy (e.g., Steinle-Neumann et al. 2001; Vočadlo et al. 2009; Wenk et al. 1988); therefore, the c/a ratio of preferentially aligned crystals of a candidate core material can be related to the anisotropy of Earth's inner core. For example, c/a ratios of iron alloys can serve as input in calculations of elastic moduli or in models of core anisotropy, as has previously been done in the case of pure hexagonal close packed (hcp) iron (e.g., Steinle-Neumann et al. 2001; Vočadlo et al. 2009).

The subsolidus phase relations and equation of state of pure iron at high pressures have been studied numerous times (e.g., Anzellini et al. 2013; Boehler et al. 2008; Dewaele et al. 2006; Jephcoat et al. 1986; Komabayashi et al. 2009; Ma et al. 2004; Mao et al. 1990; Ono et al.

47 2010; Sakai et al. 2011; Tateno et al. 2010; Uchida et al. 2001; Yamazaki et al. 2012) due to its
48 key geophysical applications. Some studies report a trend of the *c/a* ratio of hcp iron decreasing
49 with increasing pressure (Boehler et al. 2008; Dewaele et al. 2006; Jephcoat et al. 1986;
50 Yamazaki et al. 2012), while others report seemingly no trend, a very weak trend, or a trend that
51 changes with pressure (Jephcoat et al. 1986; Ma et al. 2004; Mao et al. 1990; Ono et al. 2010).
52 Similarly, some studies find that the *c/a* ratio of iron increases with increasing temperature
53 (Boehler et al. 2008; Sakai et al. 2011; Tateno et al. 2010; Yamazaki et al. 2012), in agreement
54 with most theoretical calculations (Belonoshko et al. 2003; Gannarelli et al. 2005; Modak et al.
55 2007; Sha and Cohen 2006; Steinle-Neumann et al. 2001; Wasserman et al. 1996), while others
56 do not (Ma et al. 2004). A few studies on iron (Boehler et al. 2008; Jephcoat et al. 1986) and Fe–
57 Ni–S alloy (Sakai et al. 2012) fit their room temperature data to a function describing how the
58 axial ratio changes with pressure, but it would be more useful to compile the extensive literature
59 on the *c*/*a* ratios of iron alloys into a single parameterization of their volume, temperature, and
60 compositional dependence; this is a goal of the present study.
61 Earth's inner core is known to contain several weight percent of nickel and of one or
62 more elements lighter than iron (Birch 1952; Jephcoat and Olson 1987). Silicon is one of the
63 leading candidates for comprising this light element component, based on its abundance,
64 presence in the metal of some chondritic meteorites, partitioning behavior, and non-chondritic
65 isotope ratio in the mantle (e.g., Allègre et al. 1995; McDonough 2003; Shahar et al. 2009).
66 Density functional calculations have indicated that Fe–Si hcp alloys can have significantly higher
67 elastic anisotropy than pure iron (Tsuchiya and Fujibuchi 2009), so it is important to consider the
68 composition of the alloy in addition to its structure when interpreting seismic anisotropy of the
69 inner core. Silicon-bearing alloys in the Earth's inner core may be an hcp+B2 mixture (Fischer et

al. 2013), depending on composition and temperature, which could offer an alternate explanation for anisotropy. However, the exact phase stability of the hcp+B2 mixture of Fe–Si alloys remains elusive, due to the difficulty of obtaining compositional measurements of coexisting phases in experiments at the extreme pressures and temperatures of the Earth's core.

One of the goals of the present study is to combine some of the many available datasets on the *c/a* ratio of pure iron and alloys in the Fe–Ni–Si system, to develop a single expression for the variation in *c/a* ratio as a function of volume, temperature, and composition. This parameterization can be used to calculate the compositions of the hcp component of hcp+B2 mixtures of Fe–9wt%Si (Fe–9Si) and Fe–16wt%Si (Fe–16Si) at high pressures using literature data (Fischer et al. 2012, 2014). This will allow us to put better constraints on the Fe–Si phase diagram at high pressures and temperatures, in particular the crystal structure of an Fe–Si alloy at inner core conditions, and to enhance our understanding of anisotropy in Fe–Ni–Si alloys at core conditions.

Methods

For our study of the *c/a* ratio of hcp iron, we selected numerous X-ray diffraction datasets from among the studies on the equation of state and phase relations of iron. These datasets were chosen based on their relatively smaller degree of scatter (see Discussion), the inclusion of published *c/a* ratios, and general compatibility with other modern results on the trends of the *c*/*a* ratio of iron with pressure and temperature. The studies used here consist of both diamond anvil cell (Anzellini et al. 2013; Boehler et al. 2008; Dewaele et al. 2006; Fischer et al. 2011; Ono et al. 2010; Sakai et al. 2011; Tateno et al. 2010) and multi-anvil press (Uchida et al. 2001;

92 Yamazaki et al. 2012) studies. We generally selected more recent datasets, which exhibit more
93 precise data due to improvements in experimental techniques.
94 These data were all collected using in situ synchrotron X-ray diffraction, using a variety
95 of different pressure standards and calibrations. Consideration of the pressure calibration is
96 critical when comparing results of different studies; here we largely circumvent this difficulty by
97 parameterizing *c*/*a* as a function of volume instead of pressure. In a few studies, only the
98 pressure, temperature, and *c*/*a* ratio was reported, and an equation of state was necessary to
99 determine the measured volume. Boehler et al. (2008) do not report unit cell volumes, and used
100 the ruby fluorescence pressure scale of Mao et al. (1986). We corrected their pressure
101 measurements to the ruby scale of Dorogokupets and Oganov (2007), which was calibrated
102 against the pressure scale of Dewaele et al. (2006). We then calculated the volume of iron in
103 their experiments from the corrected pressure and the reported temperature using the equation of
104 state of Dewaele et al. (2006). Likewise, Tateno et al. (2010) used the hcp iron equation of state
105 of Dubrovinsky et al. (2000) for their pressure calibration, so we used the Dubrovinsky et al.
106 (2000) equation of state to extract unit cell volumes from the pressures and temperatures reported
107 by Tateno et al. (2010).
108 To investigate the effects of nickel and silicon on the *c*/*a* ratio of hcp Fe alloys, we used
109 data from Fischer et al. (2014) on Fe–9Si, Lin et al. (2002a) on Fe–10Ni, Lin et al. (2002b) on
110 Fe–8Si, Sakai et al. (2011) on Fe–10Ni and Fe–5Ni–4Si, Komabayashi et al. (2012) on Fe–10Ni,
111 Tateno et al. (2012) on Fe–10Ni, and Tateno et al. (2015) on Fe–9Si and Fe–7Si. Lin et al.
112 (2002a, 2002b) do not report volumes, so the volumes were calculated using their reported
113 pressures and temperatures and the equations of state of pure iron (Dewaele et al. 2006) and Fe–
114 9Si (Fischer et al. 2014). The equation of state of Fischer et al. (2014) was calibrated against an

equation of state of B2 KBr (Fischer et al. 2012), which in turn was calibrated against the equation of state of Dewaele et al. (2006), so these scales should be consistent.

Results

The data we have compiled on the *c*/*a* ratio in hcp Fe–Ni–Si alloys are listed in Supplemental Table S1. It includes 928 measurements taken from 15 different studies, listing the *c*/*a* ratio, its uncertainty where available, volume, temperature, lattice parameter *a*, and mole fraction of silicon and nickel for each measurement. There are 632 measurements of pure Fe, 100 of approximately $Fe_{0.9}Ni_{0.1}$ (Fe–10Ni), 6 of $Fe_{0.88}Ni_{0.04}Si_{0.08}$ (Fe–5Ni–4Si), 10 of $Fe_{0.88}Si_{0.12}$ (Fe–6.5Si) and 180 of approximately $Fe_{0.84}Si_{0.16}$ (Fe–9Si). Data on pure Fe span ~6–340 GPa (Dewaele et al. 2006) and 300–4890 K, data on Fe–Ni alloys span ~25–340 GPa and 300–4700 K, and data on Fe–Si alloys span ~13–407 GPa and 300–5910 K.

Figure 1a shows the *c/a* ratio of pure iron from numerous studies as a function of volume and temperature (Anzellini et al. 2013; Boehler et al. 2008; Dewaele et al. 2006; Fischer et al. 2011; Ono et al. 2010; Sakai et al. 2011; Tateno et al. 2010; Uchida et al. 2001; Yamazaki et al. 2012). This figure illustrates that there is still considerable scatter within and between the datasets shown here; however, there is even greater scatter in the older datasets not chosen for inclusion in this study (e.g., Jephcoat et al. 1986; Ma et al. 2004; Mao et al. 1990). Regardless, Figure 1a demonstrates a trend of increasing *c/a* ratio with increasing volume and with increasing temperature. Similarly, the *c*/*a* ratios of hcp Fe–Ni alloys containing ~10 wt% Ni are shown in Figure 1b (Komabayashi et al. 2012; Lin et al. 2002a; Sakai et al. 2011; Tateno et al. 2012). Figure 1c shows the *c*/*a* ratio of hcp Fe–9Si where it does not coexist with any other

phases (Fischer et al. 2014; Lin et al. 2002b; Tateno et al. 2015). The *c/a* ratio in these alloys increases with both volume and temperature, similar to that of pure iron (Figure 1a).

If the axial ratio of hcp iron approaches its ideal value of 1.633 at core conditions, this could prevent anisotropy in the inner core by preferential alignment of hcp crystals (e.g., Steinle-Neumann et al. 2001). However, the data in Figure 1 indicate that the temperature dependence at inner core conditions is not strong enough for the *c/a* ratio to approach this value for pure Fe or Fe–Ni–Si alloys.

Figure 2 illustrates the *c/a* ratio of Fe–9Si changing as a function of temperature during a single heating cycle at ~145 GPa (Fischer et al. 2014). For reference, data on the *c/a* ratio of pure iron from several studies at ~130–155 GPa are also shown (Anzellini et al. 2013; Boehler et al. 2008; Fischer et al. 2011; Tateno et al. 2010). Within experimental precision, the temperature dependence of the measured axial ratio at this pressure appears to be the same for Fe–9Si and for pure Fe, since the trends in Figure 2 are parallel. The *c*/*a* ratio of the alloy is higher than that of iron by ~0.009 at these conditions.

Discussion

Axial ratios as a function of volume, temperature, and composition

The *c*/*a* ratio of an Fe–rich hcp alloy is a function of volume (V), temperature (T), and composition (X_{Si}, X_{Ni}). Using the data shown in Figure 1 and listed in Table S1, we have parameterized its dependence on these variables in the Fe–Ni–Si system as an unweighted linear fit to the data. We found the best fit to the compiled data with the following relationship:

$$c/a = 1.551 + (-2.6 \times 10^{-6})*T + 0.0094*V + (1.5 \times 10^{-6})*T*V + (4.4 \times 10^{-4})*X_{Si} + (2.8 \times 10^{-4})*X_{Ni} \quad (1)$$

with T in Kelvin, V in cm^3/mol, and X_{Si} and X_{Ni} in mole fraction (e.g., $X_{Si} = X_{Ni} = 0$ for pure iron and $X_{Si} = 16$ for Fe–9Si). The variance-covariance matrix describing this fit is shown in Supplemental Table S2. Based on the amount of scatter in the data, it was not justifiable to fit any additional terms to Equation 1; for example, allowing the temperature dependence of the *c*/*a* ratio to vary with composition did not significantly improve the quality of the fit.

Figures 1 and 2 contain curves calculated from this parameterization compared to the data. As volume increases, the *c/a* ratio increases. The *c/a* ratio always increases with increasing temperature, but this effect is strongest at higher volumes, and becomes weaker with decreasing volume. Based on the available data, we could not justify fitting any more than linear compositional terms. This implies that the axial ratios of alloys in the Fe–Ni–Si system have similar volume and temperature dependences, regardless of composition, and are simply shifted from each other based on their silicon and nickel contents.

Residuals to this fit from various studies are illustrated as a function of temperature and volume in Figure 3, which demonstrates the adequacy of Equation 1 to describe the data. The root mean squared (rms) average misfit between measured *c*/*a* ratios and those calculated from Equation 1 is 0.004 for the studies included in the fit, with the rms misfits for individual datasets ranging from 0.002 to 0.007. While these misfits are small in absolute value, they equate to ~10% of the range seen in the data. In comparison, previous studies not included in the fit due to a higher degree of scatter exhibit an estimated 2σ variation of > 0.01. The *c*/*a* ratio is likely affected by deviatoric stresses as well, which may explain the greater misfit in the 300 K data, but in this analysis we estimate that high experimental temperatures are sufficient to relax the hcp alloy and minimize deviatoric stress effects on the axial ratio.

Sakai et al. (2012) studied the effects of sulfur on the *c*/*a* ratio of hcp iron–nickel alloys at 300 K and high pressures. They found an approximately linear relationship between *c*/*a* and pressure, which is different from the trend we observe in this more extensive cross-study analysis. Their data indicate that adding 2.8 mol% S to Fe–9Ni alloy lowers the *c*/*a* ratio by ~0.005, though this varies with pressure due to the different pressure trend reported in their study.

Using the axial ratio of an Fe–Si alloy to determine its composition

Our fit to the available literature data relates the *c/a* ratio, temperature, volume, and composition of an alloy in the Fe–Ni–Si system. Therefore, in circumstances where independent measurements of the *c/a* ratio, temperature, and volume of an Fe–Si alloy are available from X-ray diffraction and spectroradiometry (or thermocouple sensor), this parameterization may be used to calculate the alloy's silicon content. In Fe–9Si and Fe–16Si, coexisting hcp+B2 structures are observed in some regions of phase space (Fischer et al. 2012, 2013). When two Fe–Si phases are present, silicon partitions between them as a function of pressure and temperature such that the compositions of the phases are unknown without sample recovery and analysis from each *P*-*T* point of interest. The method presented here provides an alternative to this restrictive process.

Figure 4 illustrates the results of this method, applied to synchrotron X-ray diffraction measurements of Fe–Si alloys at 125 and 145 GPa. At each *P*-*T* point, we have used the measured *c*/*a* ratio and Equation 1 to calculate the composition of the hcp phase that coexists with the B2 structure, thus providing the composition along the hcp to hcp+B2 phase boundary. We used data on Fe–9Si (Fischer et al. 2014) and Fe–16Si (Fischer et al. 2012), which are shown

205 in Figure 4 to be mutually consistent in their definitions of the phase boundary. The in situ
206 crossing of this phase boundary determined in Fe–9Si (Fischer et al. 2013) agrees with the
207 calculated compositions along the phase boundary within uncertainty at both pressures, verifying
208 our results. As is evident in Figure 4, this method is most useful when applied to data at
209 temperatures far from any observed phase boundary crossings, to best constrain the slope of the
210 boundary in *T*-*X* space.

211 Under experimental *P*-*T* conditions where an hcp Fe–9Si alloy does not coexist with any
212 other phase, its composition is the same as the bulk starting composition. We have compared its
213 known composition under these conditions to its composition calculated from its *c*/*a* ratio to
214 determine the precision of our method, finding a root mean square (rms) misfit of 3.9 wt%
215 silicon, based on all 147 high temperature measurements spanning 45–407 GPa (Fischer et al.
216 2014; Lin et al. 2002b; Tateno et al. 2015). We take this as an estimate of the uncertainty in the
217 calculations shown in Figure 4. The misfit might be greater at different compositions; since the
218 fit is based only on alloys with up to 9 wt% Si, we caution against its extrapolation to alloys with
219 considerably higher silicon contents.

220 Figure 4 illustrates that at temperatures approaching the eutectic temperature in the Fe–
221 FeSi system (3700(300) K at 125 GPa, 3900(300) K at 145 GPa) (Fischer et al. 2012, 2013), the
222 composition of hcp alloy that coexists with B2 alloy nearly approaches pure iron. This result is
223 consistent with ab initio studies, which find that hcp is the stable phase of iron at inner core
224 conditions but that there is a small energy difference between hcp and bcc structures, with bcc
225 stabilized by the addition of silicon (Vočadlo et al. 2003). At these pressures, eutectic melting
226 from an hcp+B2 mixture is likely over a wide range of silicon contents in Fe–Si alloys,
227 extending down to low silicon contents. The slopes we find for this phase boundary (Figure 4)

228 are slightly shallower than the boundaries reported in Fischer et al. (2013), whose slopes were
229 less well constrained. This result extends the stability of the B2 structure to lower silicon
230 contents at high temperatures, which implies that partial melting of Fe–Si alloys can produce a
231 substantial density contrast between the melt and coexisting Si-poor metal. This concept is
232 illustrated schematically in Figure S1. A 4.5–7% density contrast is observed at Earth's inner
233 core boundary (Dziewonski and Anderson 1981; Kennett et al. 1995; Masters and Gubbins
234 2003), which represents the point at which solid Fe-rich alloy crystallizes from a metallic melt.
235 At one bar the melting loop in the Fe–Si system is too narrow to explain such a large density
236 contrast, but the much larger compositional loop at high pressures, shown in this study and in
237 Fischer et al. (2013), supports the possibility that silicon could be the major light element in the
238 core, consistent with the seismological constraints.
239
240 **Calculation of the Fe–Si phase diagram in the inner core**
241 Since our parameterization of the relationship between volume, temperature, *c*/*a* ratio,
242 and silicon content spans a large *P*-*T* range up to >400 GPa and >5900 K, it can be used to
243 calculate phase boundaries at inner core conditions. The inner core is at pressures of 329–364
244 GPa (Dziewonski and Anderson 1981) and is thought to be nearly isothermal (e.g., Pozzo et al.
245 2014). The temperature of the inner core is anchored at the inner core–outer core boundary
246 (ICB), which is at the liquidus of the core's Fe-rich alloy. An extrapolation of recent results on
247 the melting of pure Fe suggest that it melts at ~6200 K at 329 GPa (Anzellini et al. 2013). At
248 pressures of 50–140 GPa, we observe a ~200 K melting point depression in Fe–Si alloys relative
249 to pure Fe (Fischer et al. 2012, 2013). Consequently, we use here an estimated ICB temperature
250 of ~6000 K for an Fe–Si core. This is an approximate lower bound on the ICB temperature of a

postulated Fe–Si core, because the melting data in the Fe–Si system are for the solidus and the inner core is crystallizing along the liquidus.

To determine the phase diagram of an Fe–Si core, we first calculated the hcp to hcp+B2 phase boundary based on experimental data from thirteen heating cycles ranging from 45 to 200 GPa. We used *c*/*a* ratios from Fischer et al. (2012, 2014), following the method described above and illustrated in Figure 4 at two different pressures. We then performed a weighted linear fit to these results, describing the relationship between pressure, temperature, and silicon content along the phase boundary. The resultant hcp to hcp+B2 boundary in the Fe–Si system is described by the equation:

$$wt\%\ Si = 16.15 - 0.00555*T + 0.0520*P \quad (2)$$

where temperature T is in Kelvin, pressure P is in GPa, and silicon content is in weight percent. A term describing the pressure dependence of the slope (constant*P*T) was not used, as it was found to be statistically insignificant at the 90% confidence level. The variance-covariance matrix describing this fit is shown in Supplemental Table S3. The rms misfit between the calculated silicon content (from Equation 1) and the fit described by Equation 2 is 2.8 wt% Si, comparable to our estimated (rms) uncertainty on the silicon content calculation. Phase boundaries calculated from Equation 2 are shown in Figure 4, illustrating compatibility with the observed phase boundary crossings in Fe–9Si. The hcp+B2 mixture is stabilized by increasing temperature, increasing silicon content, or decreasing pressure. This equation indicates that near inner core boundary conditions (329 GPa, 6000 K), an Fe–Si alloy containing greater than 0.0(21) wt% Si will be stable as a two-phase hcp+B2 mixture. For a temperature of 5500 K, an Fe–Si alloy containing greater than 2.7(19) wt% Si will be an hcp+B2 mixture. The effects of nickel on this phase boundary remain uncertain.

Figure 5 illustrates a projection of this result to inner core conditions, for an inner core temperature of 5500 K or 6000 K. At 6000 K, an Fe–Ni–Si alloy containing 6.0(7) wt% Si would match the inner core's density, based on extrapolating the equation of state of Fischer et al. (2014) and correcting for a Ni/Fe atomic ratio of 0.058 (McDonough 2003), consistent with the findings of Tateno et al. (2015). Figure 5 shows that near modern ICB conditions, the stable structure of an Fe–Si alloy with 6 wt% Si should be an hcp+B2 mixture. This phase boundary shifts to increasing silicon content with decreasing temperature, but an hcp+B2 mixture should be stable for Fe–6Si at 329 GPa for temperatures above ~4900 K.

This fit predicts a phase transition in Fe–9Si at 329 GPa and 4350(300) K. This temperature falls intermediate between extrapolations of phase boundaries from Fischer et al. (2013) and earlier studies (Lin et al. 2009; Kuwayama et al. 2009). A recent study (Tateno et al. 2015) measured the hcp/hcp+B2 phase boundary in Fe–9Si to over 400 GPa. Their phase boundary implies a transition temperature of ~4600 K at 329 GPa, in agreement with the findings of this study within uncertainty.

Implications

The axial *c*/*a* ratio in iron and Fe–Ni–Si alloys is sensitive to volume, temperature, and composition, and it has been parameterized here as a function of these variables based on a meta-analysis of experimental studies spanning a large range of pressures and temperatures. The axial ratio increases with volume, temperature, silicon content, and nickel content. The parameterization of the axial ratio as a function of these variables can be used to calculate the composition of an hcp Fe–Si alloy if its *c*/*a* ratio, temperature, and volume (or pressure) are known. Though not a substitute for direct compositional measurements, this method offers a new

297 application of equation of state data, a means to estimate the composition of the high *P*-*T* Fe–Si
298 phase in situ, and a mechanism for filling in details of phase diagrams, allowing for more robust
299 extrapolations of phase relations in pressure and temperature.

300 This parameterization allows predictions of the *c*/*a* ratio of an Fe–Ni–Si alloy of specified
301 composition at inner core conditions, which are necessary to understand the elastic anisotropy of
302 the hcp alloy (Gannarelli et al. 2005). The experiment-based parameterization presented here can
303 inform future ab initio work relating elastic constants to the *c*/*a* ratio, for a better understanding
304 of how seismic anisotropy varies with composition in hcp Fe–Ni–Si alloys.

305 The stability field of an hcp+B2 mixture in Fe–Si alloys at 125 and 145 GPa extends
306 almost to pure iron at high temperatures. This large compositional loop is consistent with silicon
307 being the light element in the Earth's core, based on seismological observations of a large
308 density contrast between the inner and outer core (Dziewonski and Anderson 1981; Kennett et al.
309 1995; Masters and Gubbins 2003). It also implies eutectic melting in the Fe–Si system over a
310 large compositional range.

311 Our calculations of the Fe–Si phase diagram suggest that if silicon is an important part of
312 the core's light element component, then a two-phase hcp+B2 mixture may be stable at inner
313 core conditions. In a two component system, there can only be two stable phases at the ICB
314 (hcp+melt), in which case the hcp structure would be stable in the inner core, but in a ternary or
315 higher order system with additional light element(s) present, hcp and B2 phases could be co-
316 crystallizing in the Earth's inner core along a cotectic. (In this case, the density contrast at the
317 ICB would be attributable mostly to the additional light element(s).) As the inner core grew, it
318 may have crystallized different compositions containing different relative amounts of hcp and B2
319 Fe–Si-rich alloy. The hcp and B2 phases have different anisotropies, so this may lead to

variations of anisotropy with depth. The ab initio simulations of Belonoshko et al. (2008) indicate a much stronger anisotropy in bcc Fe than in hcp Fe, though results of other studies (e.g., Tsuchiya and Fujibuchi 2009) are in conflict with this low anisotropy of hcp Fe. Future studies on the anisotropy of bcc-like Fe-alloys at inner core conditions are needed to clarify this issue. Similarly, it is possible that the proposed inner core translation (Alboussière et al. 2010) could cause hemispherical variations in anisotropy due to variations in phase proportion. In addition to hemispherical and radial variations in phase proportions, the hcp phase will have a different c/a ratio based on its composition and volume, with its anisotropy decreasing as the c/a ratio approaches its ideal value of 1.633. The combination of a two-phase mixture in the inner core and variations in the c/a ratio of hcp phases may help explain the observed seismic anisotropy patterns in Earth's core.

Acknowledgments

We thank Razvan Caracas for useful discussions. We are grateful to the editor for handling this manuscript and to two anonymous reviewers for constructive reviews. This work was supported by a National Science Foundation (NSF) Graduate Research Fellowship, an Illinois Space Grant Consortium Graduate Research Fellowship, an International Centre for Diffraction Data Ludo Frevel Crystallography Scholarship, and an American Association of University Women American Dissertation Fellowship to R.A.F. This work was supported by NSF grant EAR-1427123 to A.J.C.

References

342 Alboussière, T., Deguen, R., and Melzani, M. (2010) Melting-induced stratification above the
343 Earth's inner core due to convective translation. Nature, 466, 744–747.
344 Allègre, C.J., Poirier, J.-P., Humler, E., and Hofmann, A.W. (1995) The chemical composition of
345 the Earth. Earth and Planetary Science Letters, 134, 515–526.
346 Anzellini, S., Dewaele, A., Mezouar, M., Loubeyre, P., and Morard, G. (2013) Melting of iron at
347 Earth's inner core boundary based on fast X-ray diffraction. Science, 340, 464–466.
348 Belonoshko, A.B., Ahuja, R., and Johansson, B. (2003) Stability of the body-centred-cubic phase
349 of iron in the Earth's inner core. Nature, 424, 1032–1034.
350 Bergman, M.I. (1997) Measurements of electric anisotropy due to solidification texturing and the
351 implications for the Earth's inner core. Nature, 389, 60–63.
352 Birch, F. (1952) Elasticity and constitution of the Earth's interior. Journal of Geophysical
353 Research, 57, 227–286.
354 Boehler, R., Santamaría-Pérez, D., Errandonea, D., and Mezouar, M. (2008) Melting, density,
355 and anisotropy of iron at core conditions: New X-ray measurements to 150 GPa. Journal of
356 Physics: Conference Series, 121, 022018.
357 Buffett, B.A., and Wenk, H.-R. (2001) Texturing of the Earth's inner core by Maxwell stresses.
358 Nature, 413, 60–63.
359 Dewaele, A., Loubeyre, P., Occelli, F., Mezouar, M., Dorogokupets, P.I., and Torrent, M. (2006)
360 Quasihydrostatic equation of state of iron above 2 Mbar. Physical Review Letters, 97,
361 215504.
362 Dorogokupets, P.I., and Oganov, A.R. (2007) Ruby, metals, and MgO as alternative pressure
363 scales: A semiempirical description of shock-wave, ultrasonic, x-ray, and thermochemical
364 data at high temperatures and pressures. Physical Review B, 75, 024115.

365 Dubrovinsky, L.S., Saxena, S.K., Tutti, F., and Rekhi, S. (2000) In situ X-ray study of thermal
366 expansion and phase transition of iron at multimegabar pressure. Physical Review Letters,
367 84, 1720–1723.
368 Dziewonski, A.M., and Anderson, D.L. (1981) Preliminary reference Earth model. Physics of the
369 Earth and Planetary Interiors, 25, 297–356.
370 Fischer, R.A., Campbell, A.J., Shofner, G.A., Lord, O.T., Dera, P., and Prakapenka, V.B. (2011)
371 Equation of state and phase diagram of FeO. Earth and Planetary Science Letters, 304, 496–
372 502.
373 Fischer, R.A., Campbell, A.J., Caracas, R., Reaman, D.M., Dera, P., and Prakapenka, V.B.
374 (2012) Equation of state and phase diagram of Fe–16Si alloy as a candidate component of
375 Earth's core. Earth and Planetary Science Letters, 357–358, 268–276.
376 Fischer, R.A., Campbell, A.J., Reaman, D.M., Miller, N.A., Heinz, D.L., Dera, P., and
377 Prakapenka, V.B. (2013) Phase relations in the Fe–FeSi system at high pressures and
378 temperatures. Earth and Planetary Science Letters, 373, 54–64.
379 Fischer, R.A., Campbell, A.J., Caracas, R., Reaman, D.M., Heinz, D.L., Dera, P., and
380 Prakapenka, V.B. (2014) Equations of state in the Fe–FeSi system at high pressures and
381 temperatures. Journal of Geophysical Research, 119, 2810–2827.
382 Gannarelli, C.M.S., Alfè, D., and Gillan, M.J. (2005) The axial ratio of hcp iron at the conditions
383 of the Earth's inner core. Physics of the Earth and Planetary Interiors, 152, 67–77.
384 Irving, J.C.E., and Deuss, A. (2011a) Stratified anisotropic structure at the top of Earth's inner
385 core: A normal mode study. Physics of the Earth and Planetary Interiors, 186, 59–69.
386 Irving, J.C.E., and Deuss, A. (2011b) Hemispherical structure in inner core velocity anisotropy.
387 Journal of Geophysical Research, 116, B04307.

388 Ishii, M., and Dziewonski, A.M. (2002) The innermost inner core of the earth: Evidence for a
389 change in anisotropic behavior at the radius of about 300 km. Proceedings of the National
390 Academy of Sciences of the United States of America, 99, 14026–14030.
391 Ishii, M., and Dziewonski, A.M. (2003) Distinct seismic anisotropy at the centre of the Earth.
392 Physics of the Earth and Planetary Interiors, 140, 203–217.
393 Jeanloz, R., and Wenk, H.-R. (1988) Convection and anisotropy of the inner core. Geophysical
394 Research Letters, 15, 72–75.
395 Jephcoat, A., and Olson, P. (1987) Is the inner core of the Earth pure iron? Nature, 325, 332–
396 335.
397 Jephcoat, A.P., Mao, H.K., and Bell, P.M. (1986) Static compression of iron to 78 GPa with rare
398 gas solids as pressure-transmitting media. Journal of Geophysical Research, 91, 4677–4684.
399 Karato, S.-I. (1999) Seismic anisotropy of the Earth's inner core resulting from flow induced by
400 Maxwell stresses. Nature, 402, 871–873.
401 Kennett, B.L.N., Engdahl, E.R., and Buland, R. (1995) Constraints on seismic velocities in the
402 Earth from traveltimes. Geophysical Journal International, 122, 108–124.
403 Komabayashi, T., Fei, Y., Meng, Y., and Prakapenka, V. (2009) In-situ X-ray diffraction
404 measurements of the γ-ε transition boundary of iron in an internally-heated diamond anvil
405 cell. Earth and Planetary Science Letters, 282, 252–257.
406 Komabayashi, T., Hirose, K., and Ohishi, Y. (2012) In situ X-ray diffraction measurements of
407 the fcc–hcp phase transition boundary of an Fe–Ni alloy in an internally heated diamond
408 anvil cell. Physics and Chemistry of Minerals, 39, 329–338.

409 Kuwayama, Y., Sawai, T., Hirose, K., Sata, N., and Ohishi, Y. (2009) Phase relations of iron–
410 silicon alloys at high pressure and high temperature. Physics and Chemistry of Minerals, 36,
411 511–518.
412 Lin, J.-F., Heinz, D.L., Campbell, A.J., Devine, J.M., Mao, W.L., and Shen, G. (2002a) Iron–
413 nickel alloy in the Earth's core. Geophysical Research Letters, 29, 1471.
414 Lin, J.-F., Heinz, D.L., Campbell, A.J., Devine, J.M., and Shen, G. (2002b) Iron–silicon alloy in
415 Earth's core? Science, 295, 313–315.
416 Lin, J.-F., Scott, H.P., Fischer, R.A., Chang, Y.-Y., Kantor, I., and Prakapenka, V.B. (2009)
417 Phase relations of Fe–Si alloy in Earth's core. Geophysical Research Letters, 36, L06306.
418 Lythgoe, K.H., Deuss, A., Rudge, J.F., and Neufeld, J.A. (2014) Earth's inner core: Innermost
419 inner core or hemispherical variations? Earth and Planetary Science Letters, 385, 181–189.
420 Ma, Y., Somayazulu, M., Shen, G., Mao, H.-k., Shu, J., and Hemley, R.J. (2004) In situ X-ray
421 diffraction studies of iron to Earth-core conditions. Physics of the Earth and Planetary
422 Interiors, 143–144, 455–467.
423 Mao, H.K., Xu, J., and Bell, P.M. (1986) Calibration of the ruby pressure gauge to 800 kbar
424 under quasi-hydrostatic conditions. Journal of Geophysical Research, 91, 4673–4676.
425 Mao, H.K., Wu, Y., Chen, L.C., and Shu, J.F. (1990) Static compression of iron to 300 GPa and
426 $Fe_{0.8}Ni_{0.2}$ alloy to 260 GPa: Implications for composition of the core. Journal of Geophysical
427 Research, 95, 21737–21742.
428 Masters, G., and Gubbins, D. (2003) On the resolution of density within the Earth. Physics of the
429 Earth and Planetary Interiors, 140, 159–167.
430 McDonough, W.F. (2003) Compositional model for the Earth's core. In R.W. Carlson, Ed.,
431 Treatise on Geochemistry, vol. 2, p. 547–568. Elsevier-Pergamon, Oxford, U.K.

Modak, P., Verma, A.K., Rao, R.S., Godwal, B.K., Stixrude, L., and Jeanloz, R. (2007) Stability of the hcp phase and temperature variation of the axial ratio of iron near Earth-core conditions. Journal of Physics: Condensed Matter, 19, 016208.

Morelli, A., Dziewonski, A.M., and Woodhouse, J.H. (1986) Anisotropy of the inner core inferred from *PKIKP* travel times. Geophysical Research Letters, 13, 1545–1548.

Ono, S., Kikegawa, T., Hirao, N., and Mibe, K. (2010) High-pressure magnetic transition in hcp-Fe. American Mineralogist, 95, 880–883.

Poupinet, G., Pillet, R., and Souriau, A. (1983) Possible heterogeneity of the Earth's core deduced from PKIKP travel times. Nature, 305, 204–206.

Pozzo, M., Davies, C., Gubbins, D., and Alfè, D. (2014) Thermal and electrical conductivity of solid iron and iron–silicon mixtures at Earth's core conditions. Earth and Planetary Science Letters, 393, 159–164.

Reaman, D.M., Daehn, G.S., and Panero, W.R. (2011) Predictive mechanism for anisotropy development in the Earth's inner core. Earth and Planetary Science Letters, 312, 437–442.

Sakai, T., Ohtani, E., Hirao, N., and Ohishi, Y. (2011) Stability field of the hcp-structure for Fe, Fe–Ni, and Fe–Ni–Si alloys up to 3 Mbar. Geophysical Research Letters, 38, L09302.

Sakai, T., Ohtani, E., Kamada, S., Terasaki, H., and Hirao, N. (2012) Compression of $Fe_{88.1}Ni_{9.1}S_{2.8}$ alloy up to the pressure of Earth's inner core. Journal of Geophysical Research, 117, B02210.

Sha, X., and Cohen, R.E. (2006) Thermal effects on lattice strain in ε-Fe under pressure. Physical Review B, 74, 064103.

453 Shahar, A., Ziegler, K., Young, E.D., Ricolleau, A., Schauble, E.A., and Fei, Y. (2009)
454 Experimentally determined Si isotope fractionation between silicate and Fe metal and
455 implications for Earth's core formation. Earth and Planetary Science Letters, 288, 228–234.
456 Steinle-Neumann, G., Stixrude, L., Cohen, R.E., and Gülseren, O. (2001) Elasticity of iron at the
457 temperature of the Earth's inner core. Nature, 413, 57–60.
458 Stixrude, L., and Cohen, R.E. (1995) High-pressure elasticity of iron and anisotropy of Earth's
459 inner core. Science, 267, 1972–1975.
460 Tanaka, S., and Hamaguchi, H. (1997) Degree one heterogeneity and hemispherical variation of
461 anisotropy in the inner core from PKP(BC)–PKP(DF) times. Journal of Geophysical
462 Research, 102, 2925–2938.
463 Tateno, S., Hirose, K., Ohishi, Y., and Tatsumi, Y. (2010) The structure of iron in Earth's inner
464 core. Science, 330, 359–361.
465 Tateno, S., Hirose, K., Komabayashi, T., Ozawa, H., and Ohishi, Y. (2012) The structure of Fe–
466 Ni alloy in Earth's inner core. Geophysical Research Letters, 39, L12305.
467 Tateno, S., Kuwayama, Y., Hirose, K., and Ohishi, Y. (2015) The structure of Fe–Si alloy in
468 Earth's inner core. Earth and Planetary Science Letters, 418, 11–19.
469 Tsuchiya, T., and Fujibuchi, M. (2009) Effects of Si on the elastic property of Fe at Earth's inner
470 core pressures: First principles study. Physics of the Earth and Planetary Interiors, 174, 212–
471 219.
472 Uchida, T., Wang, Y., Rivers, M.L., and Sutton, S.R. (2001) Stability field and thermal equation
473 of state of ε-iron determined by synchrotron X-ray diffraction in a multianvil apparatus.
474 Journal of Geophysical Research, 106, 21799–21810.

475 Vočadlo, L., Alfè, D., Gillan, M.J., Wood, I.G., Brodholt, J.P., and Price, G.D. (2003) Possible
476 thermal and chemical stabilization of body-centered-cubic iron in the Earth's core. Nature,
477 424, 536–539.
478 Vočadlo, L., Dobson, D.P., and Wood, I.G. (2009) Ab initio calculations of the elasticity of hcp-
479 Fe as a function of temperature at inner-core pressure. Earth and Planetary Science Letters,
480 288, 534–538.
481 Wasserman, E., Stixrude, L., and Cohen, R.E. (1996) Thermal properties of iron at high
482 pressures and temperatures. Physical Review B, 53, 8296–8309.
483 Wenk, H.R., Takeshita, T., Jeanloz, R., and Johnson, G.C. (1988) Development of texture and
484 elastic anisotropy during deformation of hcp metals. Geophysical Research Letters, 15, 76–
485 79.
486 Yamazaki, D., Ito, E., Yoshino, T., Yoneda, A., Guo, X., Zhang, B., Sun, W., Shimojuku, A.,
487 Tsujino, N., Kunimoto, T., Higo, Y., and Funakoshi, K.-i. (2012) *P-V-T* equation of state for
488 ε-iron up to 80 GPa and 1900 K using the Kawai-type high pressure apparatus equipped with
489 sintered diamond anvils. Geophysical Research Letters, 39, L20308.
490 Yoshida, S., Sumita, I., and Kumazawa, M. (1996) Growth model of the inner core coupled with
491 the outer core dynamics and the resulting elastic anisotropy. Journal of Geophysical
492 Research, 101, 28085–28103.
493

494 **Figure Captions:**

495 Figure 1: Axial ratio of hcp Fe–Ni–Si alloys as a function of volume and temperature. A: Pure
496 hcp iron. Filled diamonds: Anzellini et al. (2013). Filled squares: Boehler et al. (2008). Filled
497 triangles: Fischer et al. (2011). Filled circles: Yamazaki et al. (2012). Open diamonds: Ono et al.

(2010). Open squares: Tateno et al. (2010). Open triangles: Uchida et al. (2001). Open circles: Sakai et al. (2011). × symbols: Dewaele et al. (2006). B: Fe–10Ni alloy. Filled diamonds: Tateno et al. (2012). Filled squares: Lin et al. (2002a). Filled triangles: Komabayashi et al. (2012). Filled circles: Sakai et al. (2011). C: Fe–9Si alloy. Filled diamonds: Fischer et al. (2014). Filled circles: Lin et al. (2002b). Filled triangles: Tateno et al. (2015). All data are color-coded by temperature according to the legend. Curves are calculated from Equation 1, and are shown for the midpoints of the indicated temperature ranges. In part A, they are truncated to not extend outside the stability field of hcp iron (Anzellini et al. 2013; Komabayashi et al. 2009). Error bars are not shown because some studies did not report uncertainties, but they are typically in the range 0.02 to 0.3% for the *c*/*a* ratio.

Figure 2: Measured *c*/*a* axial ratio of Fe–9Si compared to that of pure iron as a function of temperature. Data on Fe–9Si (grey symbols) are from a heating cycle at ~145 GPa (Fischer et al. 2014). Data on pure iron (black symbols) span ~130–155 GPa. Iron data come from a variety of studies (Anzellini et al. 2013; Boehler et al. 2008; Fischer et al. 2011; Tateno et al. 2010), with a single heating cycle shown from each study. Lines are calculated for 145 GPa (based on equations of state of Dewaele et al. (2006) and Fischer et al. (2014)) from Equation 1 (solid line: Fe–9Si; dashed line: pure iron). The trends of the data are parallel, indicating that the *c/a* ratios of Fe–9Si and pure iron have similar temperature dependences at this pressure.

Figure 3: Residuals to Equation 1. Symbols are as in Figure 1. A: Pure hcp iron. B: Fe–10Ni alloy. C: Fe–9Si alloy. All data are color-coded by temperature according to the legend.

Figure 4: Phase boundaries in the Fe–FeSi system calculated using the *c/a* ratio of intermediate alloys at A: ~125 GPa and B: ~145 GPa. Each data point represents an observation of coexisting hcp and B2 structures in either Fe–9Si (blue diamonds) or Fe–16Si (orange open circles). Data are from Fischer et al. (2012, 2014). The *c/a* ratio of the hcp phase was used to calculate its composition along the phase boundary using Equation 1. Black crosses indicate upper and lower bounds on the transition for Fe–9Si based on in situ X-ray diffraction measurements (Fischer et al. 2013). Solid black lines are phase boundaries calculated from Equation 2; dashed lines are 95% confidence intervals. Error bars in composition are a root mean square misfit.

Figure 5: Phase diagram of Fe–Si alloys in the inner core, calculated using Equation 2 and shown in pressure-composition space at a fixed temperature of 6000 K (black lines) or 5500 K (grey lines). Solid lines: hcp to hcp+B2 phase boundary. Dashed lines: amount of silicon needed to match the inner core's density at these conditions (Fischer et al. 2014). Yellow bands indicate uncertainties at 6000 K. If silicon is the core's dominant light element, the inner core may be a mixture of hcp and B2 phases.

Supplemental Table Captions:

Table S1: Compilation of *c*/*a* ratios from 15 studies, as a function of temperature, volume, lattice parameter *a*, and mole fractions of Ni and Si. Uncertainties on the *c*/*a* ratio are listed where available.

Table S2: Variance-covariance matrix describing the fit of c/a as a function of T, V, and composition (Equation 1), with T in Kelvin, V in cm^3/mol, and X_{Si} and X_{Ni} in mole fraction. Diagonal terms describe the variance in each coefficient, while off-diagonal terms describe the covariance between terms. Matrix is symmetric by definition.

Table S3: Variance-covariance matrix describing the silicon content along the hcp to hcp+B2 phase boundary in the Fe–Si system as a function of T and P (Equation 2), with silicon content in weight percent, T in Kelvin, and P in GPa. Diagonal terms describe the variance in each coefficient, while off-diagonal terms describe the covariance between terms. Matrix is symmetric by definition.

Supplemental Figure Caption:

Figure S1: Schematic temperature-composition phase diagrams in the Fe–Si system. A: A wide hcp+B2 two-phase field (red arrow), as shown in this study, allows for a larger compositional contrast (blue arrow) between coexisting solid and melt at inner core boundary pressures. This makes it possible for a Si-rich core to be compatible with seismic observations of a large density contrast between the inner and outer core (e.g., Masters and Gubbins 2003). B: In contrast, a narrow two-phase field would preclude the possibility of a large compositional contrast between coexisting solid and melt in the Fe–Si system, making silicon a less viable candidate for the core's dominant light element.

Figure 1

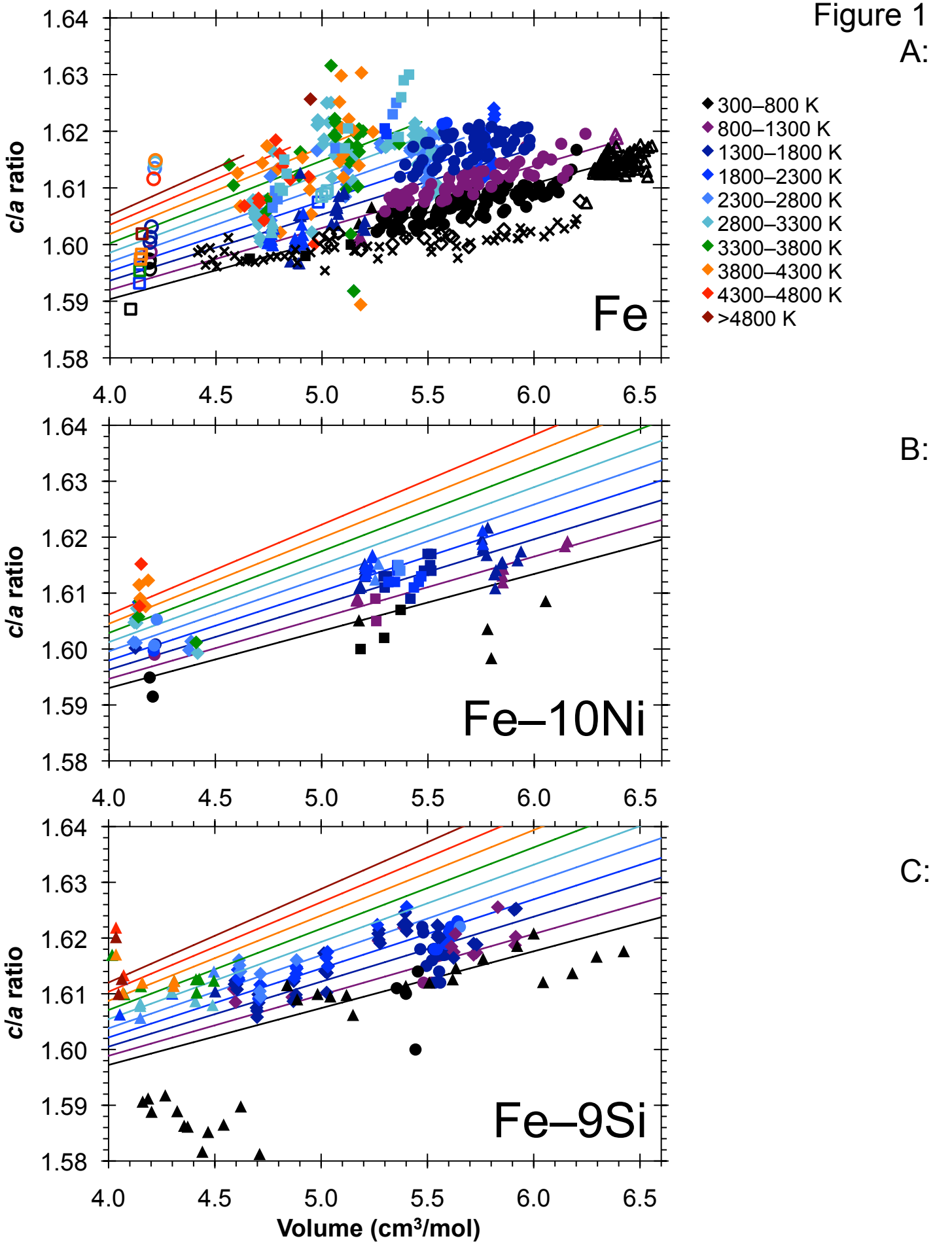
A:
B:
C:
c/a ratio
1.64
1.63
1.62
1.61
1.60
1.59
1.58
4.0
4.5
5.0
5.5
6.0
6.5
Volume (cm³/mol)
300–800 K
800–1300 K
1300–1800 K
1800–2300 K
2300–2800 K
2800–3300 K
3300–3800 K
3800–4300 K
4300–4800 K
>4800 K
Fe
Fe–10Ni
Fe–9Si

Figure 2

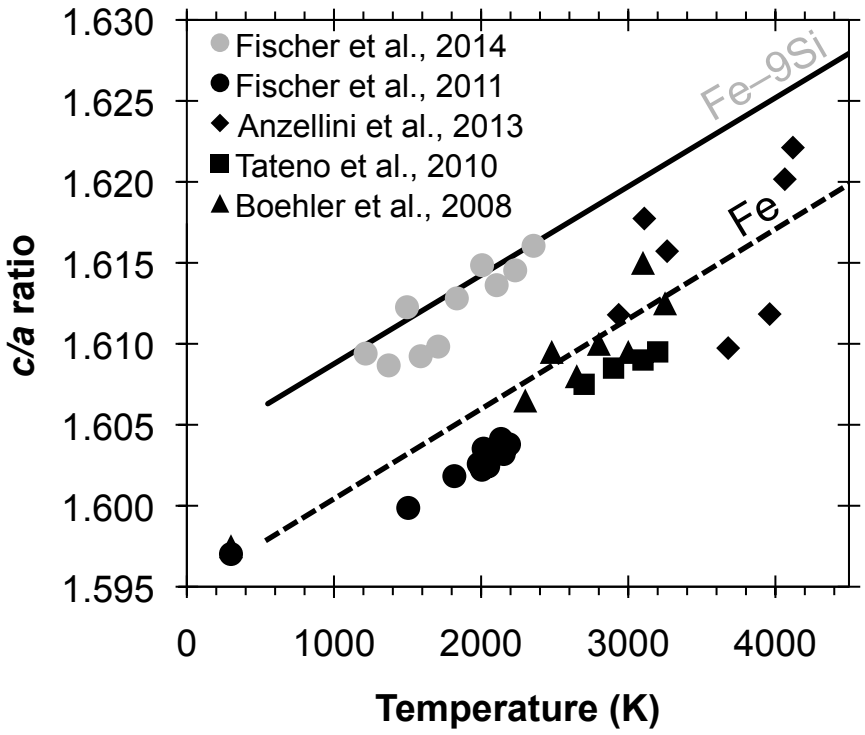
1.630
1.625
1.620
1.615
1.610
1.605
1.600
1.595
c/a ratio
0
1000
2000
3000
4000
Temperature (K)
Fischer et al., 2014
Fischer et al., 2011
Anzellini et al., 2013
Tateno et al., 2010
Boehler et al., 2008
Fe–9Si
Fe

Figure 3

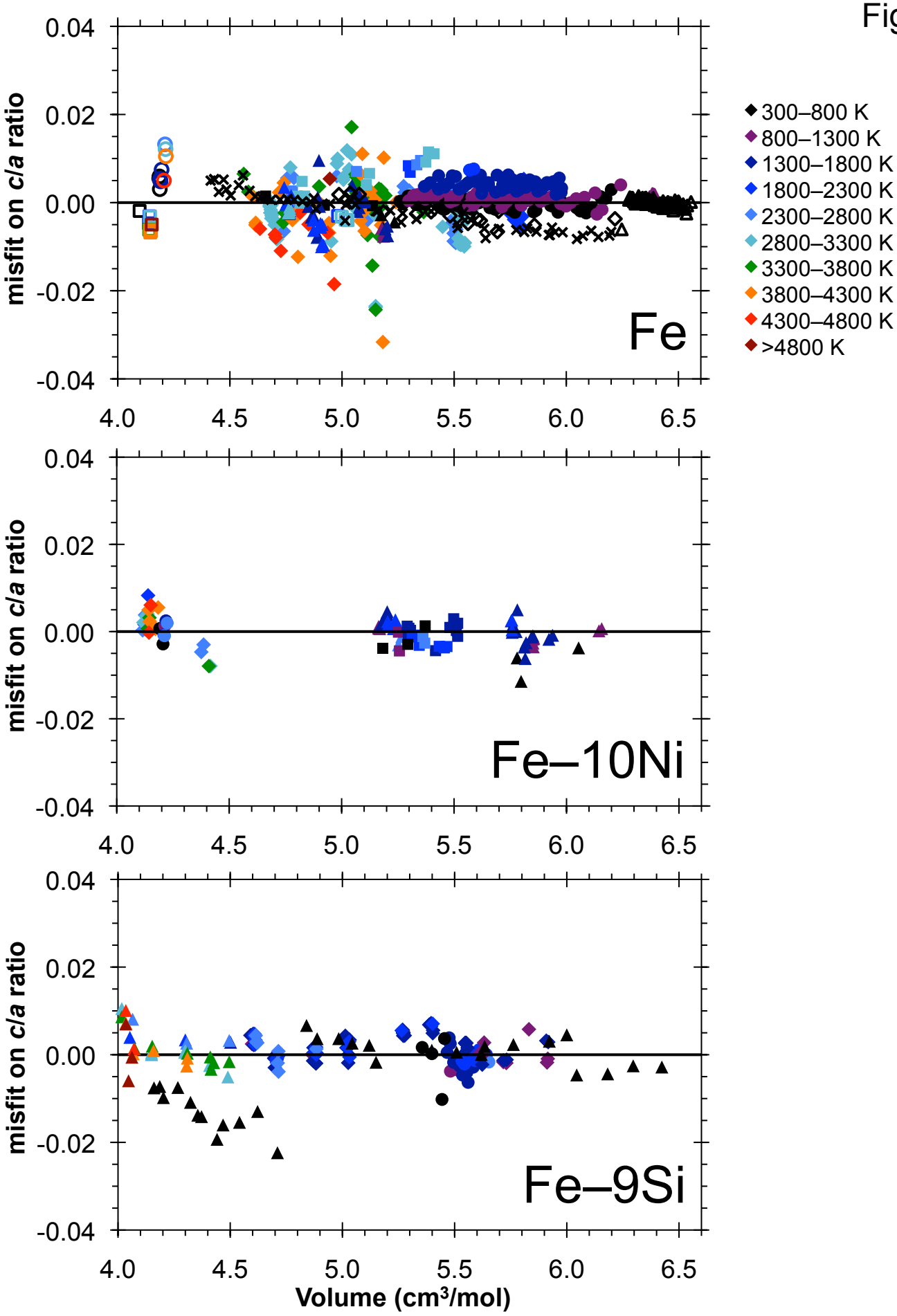
A:
B:
C:
misfit on c/a ratio
0.04
0.02
0.00
-0.02
-0.04
4.0
4.5
5.0
5.5
6.0
6.5
Fe
Fe–10Ni
Fe–9Si
300–800 K
800–1300 K
1300–1800 K
1800–2300 K
2300–2800 K
2800–3300 K
3300–3800 K
3800–4300 K
4300–4800 K
>4800 K
Volume (cm³/mol)

Figure 4

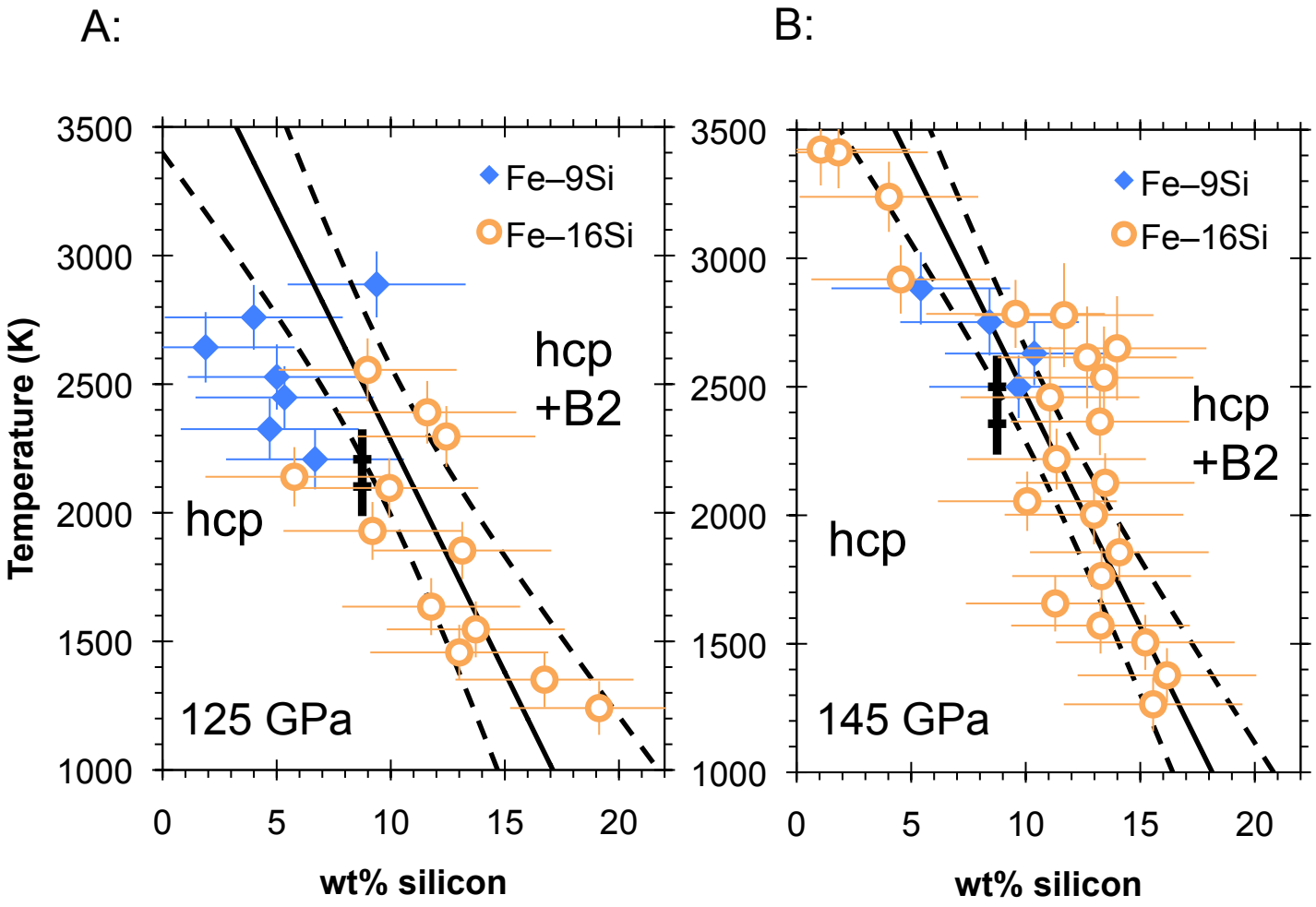
A:
B:
Temperature (K)
3500
3000
2500
2000
1500
1000
0
5
10
15
20
wt% silicon
Fe–9Si
Fe–16Si
hcp
hcp
+B2
125 GPa
145 GPa

Figure 5

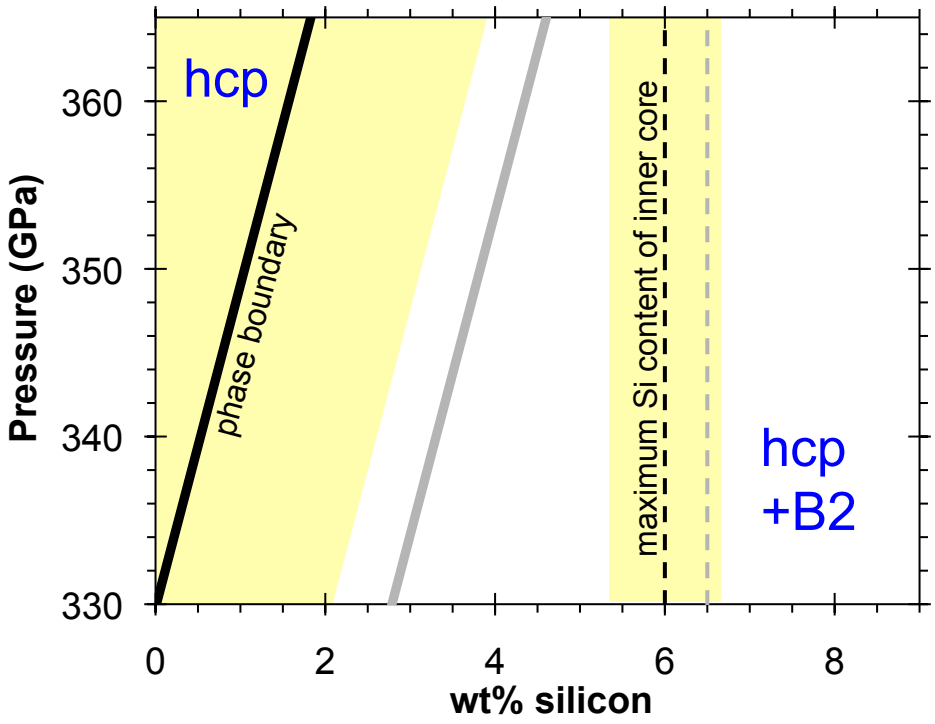
hcp
phase boundary
maximum Si content of inner core
hcp
+B2
Pressure (GPa)
360
350
340
330
0
2
4
6
8
wt% silicon